



Dynamic structural and microstructural responses of a metal–organic framework type material to carbon dioxide under dual gas flow and supercritical conditions

Andrew J. Allen, Eric Cockayne, Winnie Wong-Ng, Jeffrey T. Culp and Ivan Kuzmenko

J. Appl. Cryst. (2023). **56**, 222–236



IUCr Journals
CRYSTALLOGRAPHY JOURNALS ONLINE

Author(s) of this article may load this reprint on their own web site or institutional repository and on not-for-profit repositories in their subject area provided that this cover page is retained and a permanent link is given from your posting to the final article on the IUCr website.

For further information see <https://journals.iucr.org/services/authorrights.html>

Received 4 January 2022
 Accepted 23 December 2022

Edited by H. Brand, Australian Synchrotron,
 ANSTO, Australia

Keywords: X-ray diffraction; XRD; small-angle X-ray scattering; SAXS; density functional theory; DFT; dual gas sorption; supercritical CO₂ adsorption; metal–organic framework materials; MOFs; PICNIC class solid sorbents; carbon dioxide reduction; CDR.

Supporting information: this article has supporting information at journals.iucr.org/j

Dynamic structural and microstructural responses of a metal–organic framework type material to carbon dioxide under dual gas flow and supercritical conditions

Andrew J. Allen,^{a,*} Eric Cockayne,^a Winnie Wong-Ng,^a Jeffrey T. Culp^{b,c} and Ivan Kuzmenko^d

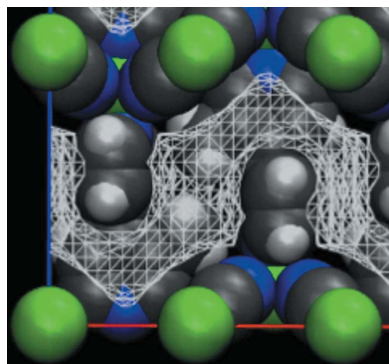
^aMaterials Measurement Science Division, National Institute of Standards and Technology, 100 Bureau Drive, Gaithersburg, MD 20899, USA, ^bLRST/Battelle, NETL, Pittsburgh, PA 15236, USA, ^cNational Energy Technology Laboratory, US Department of Energy, Pittsburgh, PA 15236, USA, and ^dX-ray Science Division, Argonne National Laboratory, 9700 South Cass Avenue, Argonne, IL 60439, USA. *Correspondence e-mail: andrew.allen@nist.gov

The structural and microstructural responses of a model metal–organic framework material, Ni(3-methyl-4,4'-bipyridine)[Ni(CN)₄] (Ni-BpyMe or PICNIC-21), to CO₂ adsorption and desorption are reported for *in situ* small-angle X-ray scattering and X-ray diffraction measurements under different gas pressure conditions for two technologically important cases. These conditions are single or dual gas flow (CO₂ with N₂, CH₄ or H₂ at sub-critical CO₂ partial pressures and ambient temperatures) and supercritical CO₂ (with static pressures and temperatures adjusted to explore the gas, liquid and supercritical fluid regimes on the CO₂ phase diagram). The experimental results are compared with density functional theory calculations that seek to predict where CO₂ and other gas molecules are accommodated within the sorbent structure as a function of gas pressure conditions, and hence the degree of swelling and contraction in the associated structure spacings and void spaces. These predictions illustrate the insights that can be gained concerning how such sorbents can be designed or modified to optimize the desired gas sorption properties relevant to enhanced gas recovery or to addressing carbon dioxide reduction through carbon mitigation, or even direct air capture of CO₂.

1. Introduction

For many years there has been an ongoing and growing research interest in the design and development of new solid gas sorbent materials that can adjust their structures to accommodate high densities of adsorbed gas solvent molecules (Yaghi *et al.*, 2003; Férey, 2008; Ferreira *et al.*, 2020). This is motivated by commercial and societal needs for molecular sorption and gas detection, enhanced oil or gas recovery, various other gas storage or separation applications, and a need for increasingly efficient (and inexpensive) gas sorbent materials to address climate change through carbon dioxide reduction (CDR), encompassing carbon capture, utilization and storage (CCUS) (Adil *et al.*, 2017; Trickett *et al.*, 2017). In this context, metal–organic frameworks (MOFs), containing metal ions or clusters linked into highly porous 3D networks by coordinated organic ligands, remain of great interest (Bennett & Cheetham, 2014; Coudert, 2015).

Among MOFs, flexible porous coordination polymers (PCPs) show promise because of their ability to exhibit hysteresis in reversible structural transitions between low- and



high-porosity states during gas sorption cycles (Culp, Sui *et al.*, 2013; Banerjee *et al.*, 2016).

One group of microporous compounds possessing such MOF-like structures is the pillared cyanonickelate ('PICNIC') family of Hofmann compounds (Hofmann & Küspert, 1897; Hagrman *et al.*, 1999), based on square-planar sheets of Ni(CN)₂ bridged by organic ligands terminated by N atoms at each end. Since the network is not inherently rigid against shearing of the Ni(CN)₂ planes with respect to each other, some PICNIC materials are flexible, although not all (Culp, Madden *et al.*, 2013). Well over 40 PICNIC family members have been synthesized by incorporating different ligand combinations *etc.*, and some of the present authors have determined the structures of several of these compounds (Kaufman *et al.*, 2011; Wong-Ng *et al.*, 2013; Allen *et al.*, 2015; Wong-Ng *et al.*, 2016). Previously, we have used a combination of experimental *in situ* simultaneous small-angle X-ray scattering (SAXS) and wide-angle X-ray scattering (WAXS) X-ray diffraction (XRD) measurements with density functional theory (DFT) calculations to investigate the structural changes that occur in PICNIC-60, known as Ni-Bpene, during CO₂ adsorption (Allen *et al.*, 2018). This flexible member of the PICNIC family exhibits hysteresis in its CO₂ adsorption/desorption isotherms and step changes that can be associated with structural changes to accommodate (or release) CO₂ molecules. It was established that rotations of the Bpene ligands occur as the structure goes from low CO₂ filling to maximum CO₂ uptake, along with a significant expansion in the unit cell.

Here, we focus on another member of the PICNIC family: PICNIC-21, known as Ni-BpyMe, with the composition Ni(3-methyl-4,4'-bipyridine)[Ni(CN)₄]. Unlike Ni-Bpene, the CO₂ sorption isotherms of Ni-BpyMe show a Type I isotherm (Sing, 1985), with CO₂ uptake commencing at low pressures and no hysteresis exhibited between the CO₂ adsorption and desorption isotherm branches (see Fig. S1 in the supporting information). Hence, Ni-BpyMe does not nominally exhibit the flexible PCP behavior of Ni-Bpene, and the basic structure appears to change only incrementally during gas adsorption and desorption. However, this does not mean that changes in lattice spacing are absent in the presence of adsorbed guest molecules, as has been shown in single-crystal XRD measurements that compared Ni-BpyMe containing dimethyl sulfoxide (DMSO) guest molecules with its subsequent guest-free state following acetone solvent extraction and evacuation (Wong-Ng *et al.*, 2021). That study achieved a structural refinement of the guest-free crystalline framework of Ni-BpyMe. Also, we have previously used DFT calculations and analysis to elucidate how the local structure of sorbent-free Ni-BpyMe differs from its average structure, as well as the importance of dispersion interactions in this system (Cockayne *et al.*, 2021).

Unfortunately, it has not proved possible to conduct *a priori* single-crystal determinations of the flexible Ni-BpyMe structure under the realistic gas pressure conditions of interest in CDR. Nevertheless, in this paper we have extended the experimental measurements using *in situ* SAXS and WAXS

(powder XRD), together with performing further DFT calculations, to follow the microstructural and structural responses of Ni-BpyMe to gas adsorption under two technologically important gas pressure conditions. One of these cases comprises single and dual gas flow conditions using CO₂, CO₂/N₂, CH₄, CO₂/CH₄, H₂ and CO₂/H₂ at ambient temperatures, and approximates to some of the conditions encountered in attempts to separate CO₂ from a concentrated process gas stream. The other scenario is an exploration of the CO₂ phase diagram for adsorbed CO₂ in Ni-BpyMe as a function of (static) pressure and temperature around the CO₂ critical point to determine how far the Ni-BpyMe structure can adjust to accommodate CO₂ molecules for maximum adsorption.

Through studies of how the microstructural and structural responses of this PICNIC compound depend on ligand configuration, and how this structure in turn affects the gas adsorption properties, we seek to demonstrate the use of such combined studies to provide a basis for engineering PICNICs (and other MOFs) to target optimized gas adsorption properties, especially with regard to the adsorption and retention of CO₂ in support of CDR objectives, and even for direct air capture (DAC) of CO₂.

2. Materials and methods

2.1. Sample preparation

The Ni-BpyMe powder sample preparation has been detailed previously (Wong-Ng *et al.*, 2016, 2021). Briefly, a 50 ml flask was filled at room temperature with polymeric nickel cyanide hydrate, Ni[Ni(CN)₄]_n·3H₂O (0.5 mmol l⁻¹), which was dissolved through sequential additions of H₂O (6 ml), reagent-concentrated NH₄OH solution (6 ml) and dimethyl sulfoxide (DMSO; 9 ml) with stirring. A solution of BpyMe (0.5 mmol l⁻¹) in warm DMSO (9 ml) was then added to the resulting solution. A 150 mm diameter air-cooled condenser was added and the flask transferred to an oil bath preheated to 343 K (70°C). The temperature of the oil bath was ramped up to 363 K (90°C) over ~30 min, after which stirring was stopped and the reaction left undisturbed at 90°C for 2 d. The dissolved NH₃ bubbled out of the solution rapidly during the initial hour, and then slowed significantly while a crystalline product formed over the next two days. On completion, the mixture was cooled to room temperature and the resulting crystals isolated by decanting off any suspended fine particle impurities, while ensuring the crystals remained wet within the reaction mixture. Impurities were removed by filtration and the filtrate returned to the flask. This pipetting and filtration cycle was repeated until all powdered impurities were removed. The residual light-violet crystals were stored in the cleaned reaction mixture in a capped vial at room temperature until sample mounting for the X-ray measurements described below.

2.1.1. Structure of Ni-BpyMe (PICNIC-21). The structure of Ni-BpyMe has been refined using single-crystal XRD measurements (Wong-Ng *et al.*, 2016). Following the DMSO fabrication route summarized above, it was found to have a

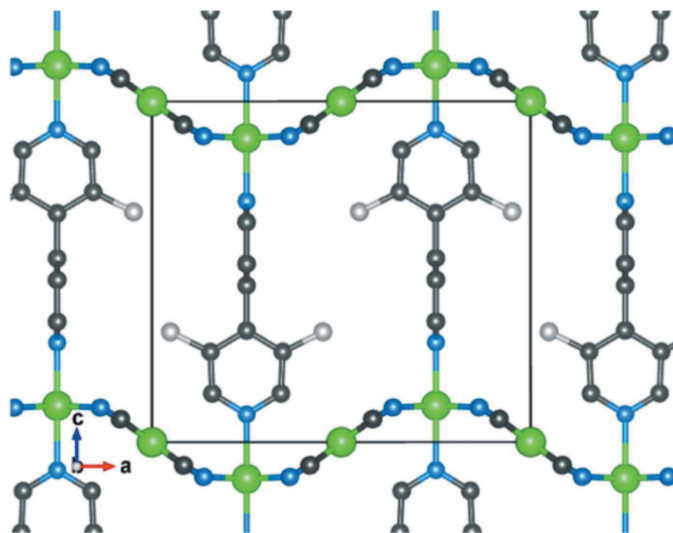


Figure 1

The average structure of Ni-BpyMe, as determined from XRD refinement. Color code: Ni atoms are shown in green, C dark gray and N blue. H atoms have been omitted for clarity. Light-gray sites are carbon positions with 0.5 occupancy, indicating that the methyl group of an individual ligand points in either the x or the $-x$ direction. Pyridine rings without methyl groups appear edge on. Coordinates show the x (a) and z (c) directions. The box indicates the a_0 and c_0 unit-cell parameters.

monoclinic structure with space group $P2_1/n$. However, a more recent single-crystal XRD study (Wong-Ng *et al.*, 2021)¹ has shown that, after removal of DMSO guest molecules using acetone solvent extraction and then evacuation, significant changes in the bipyridyl dihedral angle cause a change in structure to orthorhombic with space group $Pmma$ and guest-free lattice spacings: $a_0 = 12.603 \text{ \AA}$, $b_0 = 7.332 \text{ \AA}$, $c_0 = 11.310 \text{ \AA}$ and unit-cell volume $V = 1045 \text{ \AA}^3$, containing $Z = 2$ formula units. The orthorhombic structure also exhibits a Type I isotherm for gas adsorption. This single-crystal XRD and DFT study showed that, instead of the methyl group being in one position on the pyridine ring, it has an equal (50%) chance of being in two mirror-related positions on the same pyridine ring. These and other aspects of the Ni-BpyMe structural arrangement can impinge on its gas sorption properties, as elucidated in DFT studies (Cockayne *et al.*, 2021) to be discussed in connection with the present results. Based on this recent work, a schematic diagram of the guest-free Ni-BpyMe structure is shown for information in Fig. 1 to aid our later discussion of the present results. Sorbent molecules will primarily inhabit the $x0z$ plane.

2.2. SAXS and WAXS characterization

Combined *in situ* ultra-small-angle X-ray scattering (USAXS), SAXS and WAXS (XRD) measurements were made on powdered Ni-BpyMe samples, under the gas pressure

and temperature conditions described below, using the USAXS facility at sector 9-ID-C of the Advanced Photon Source (APS), Argonne National Laboratory, Argonne, Illinois, USA. This facility, together with the gas sorption sample environments used here, is described elsewhere (Ilavsky *et al.*, 2018). Using this facility, USAXS, SAXS and WAXS data can be obtained in less than 6 min without disturbing the sample environment. Scattering or diffracted intensity data, $I(q)$, were measured as a function of q , where $q = (4\pi/\lambda)\sin\theta$, λ is the X-ray wavelength (0.5904 \AA for the 21 keV X-rays used), and θ is one-half of the scattering or diffraction angle. Slit-smear USAXS, SAXS and WAXS data were reduced and their absolute intensities calibrated using the USAXS facility suite computer programs for data reduction and analysis: *Indra*, *Irena* and *Nika*, written in *Igor Pro* (WaveMetrics Inc., Lake Oswego, Oregon, USA)² as described elsewhere (Ilavsky & Jemian, 2009; Ilavsky, 2012). For each combined USAXS/SAXS/WAXS data set, $I(q)$ versus q data were obtained over a q range from 0.0001 \AA^{-1} to (nominally) $>6 \text{ \AA}^{-1}$ with $\Delta q/q$ resolution typically ~ 0.025 for USAXS, ~ 0.008 for SAXS and ~ 0.003 for WAXS. This overall q range accommodates both much of the Ni-BpyMe XRD pattern and microstructure scales from $\sim 10 \text{ \AA}$ to a few micrometres. In practice, sample cell shielding reduces the maximum achievable q to $\sim 4.5 \text{ \AA}^{-1}$, while the XRD range of most interest here is 0.5 to $\sim 2 \text{ \AA}^{-1}$.

The combined USAXS/SAXS parts of the reduced and calibrated data sets were subjected to a scattering feature size distribution analysis using the entropy maximization technique, MaxEnt (Potton *et al.*, 1988), to determine significant changes in the volume fraction size distribution of voids in the morphology during gas adsorption and desorption. To accomplish this, the scattering contrast factor between the gas or fluid in the void spaces and the solid Ni-BpyMe matrix (with appropriate loading of adsorbed gas molecules) needed to be calculated for each measurement condition, especially for the supercritical CO_2 sorption studies discussed later (Table S1). For the powder samples used in these studies, the coarsest micrometre-scale component in the size distribution captured by MaxEnt was attributed to gaps between the powder grains. This component was excluded from further analysis. The volume fractions of the remaining parts of the size distribution, namely nanoscale pores and a broad distribution of coarser mesoscale voids, were re-normalized to the volume remaining after removal of this coarse component, thus providing volume fraction information more intrinsic to the Ni-BpyMe sorbent without the influence of powder packing. Fig. 2(a) presents typical USAXS/SAXS data and some representative MaxEnt pore volume fraction size distributions. Meanwhile, selected XRD peaks in the WAXS part of each data set were fitted assuming a Lorentzian XRD peak shape, using the diffraction peak fitting algorithms in the

¹ Cambridge Structural Database (CSD; Groom *et al.*, 2016) refcode ANUZOB (CCDC 2046166) contains the supplementary crystallographic data for Ni-BpyMe. These data can be obtained free of charge via <http://www.ccdc.cam.ac.uk>, or from the Cambridge Crystallographic Data Centre, 12 Union Road, Cambridge CB2 1EZ, UK; fax: (+44) 1223 336 033; e-mail: deposit@ccdc.cam.ac.uk.

² Certain commercial instruments, materials, software or processes are identified in this paper to specify the experimental procedure adequately. Such identification does not imply recommendation or endorsement by the National Institute of Standards and Technology, nor does it imply that the instruments, materials or processes identified are necessarily the best available for the purpose.

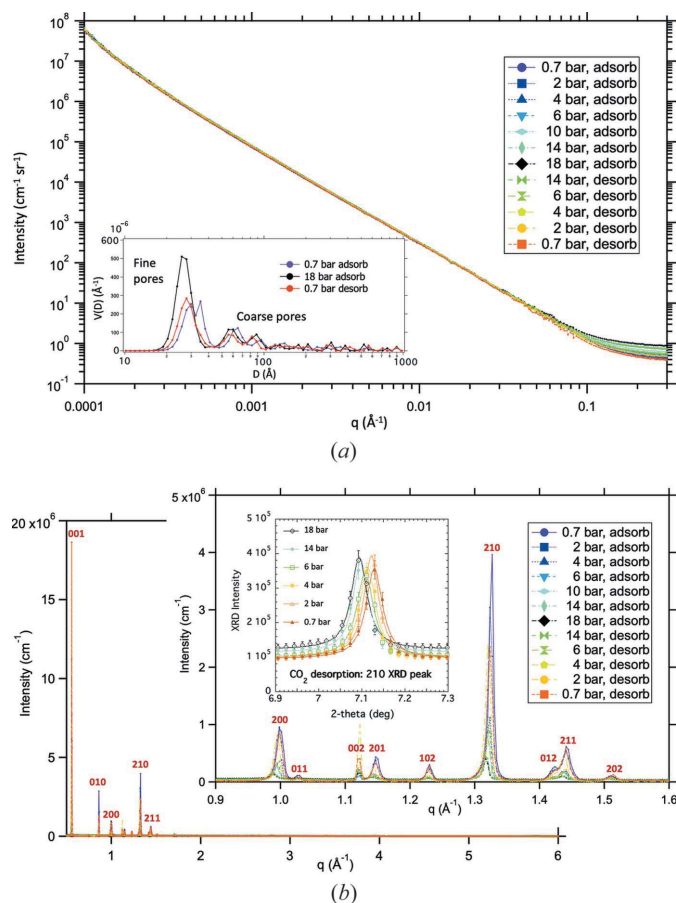


Figure 2
 (a) Combined slit-smear USAXS/SAXS data for pure CO₂ gas flow adsorption to 1.8 MPa (18 bar) and desorption from/to below atmospheric pressure, together with MaxEnt volume fraction size distributions, $V(D)$ versus diameter D , with fine (nanoscale) and coarser mesoscale pores indicated. Measurement uncertainties in the main plot have been omitted for clarity. (b) Associated SAXS/WAXS (XRD) data versus q , with magnification of the range of interest and a further inset showing an example 210 XRD peak analysis. Vertical bars in the inset represent detector intensity standard uncertainties.

Irena Igor Pro analysis package (Ilavsky & Jemian, 2009). Fig. 2(b) shows typical XRD data and examples of peak fitting, giving the results discussed later. See also Fig. S2 and associated discussion in the supporting information.

2.2.1. Measurements under dual gas flow conditions. For gas flow measurements, a small quantity of Ni-BpyMe powder was removed from the storage vial mentioned above and pressed between two layers of adhesive polypropylene film tape, perforated to allow inflow and outflow of gas. The encapsulated sample was mounted in a custom-designed pressure cell with polyamide film windows. This cell was connected to an automated Hiden XCS dual gas flow system (Hiden Isochema Ltd, Warrington, UK). This system provides gas flow through the sample at ~ 100 ml min⁻¹ and a gate valve arrangement to apply total gas pressures up to 5 MPa (50 bar) at room temperature, as reported previously (Ilavsky *et al.*, 2018; Allen *et al.*, 2018). After initial sample activation by applying a CO₂ pressure of 0.5 MPa (5 bar), followed by partial evacuation to ~ 0.03 MPa (0.3 bar), USAXS, SAXS

Table 1

Summary of single and dual gas flow measurement conditions.

All measurements were taken at ambient temperature and a total nominal flow rate of 100 ml min⁻¹. Dual gas flows have a 50:50 gas flow mix after gas law corrections. CO₂ partial pressures are half of the total pressure for dual gas cases, where 1 bar = 0.1 MPa. Measurements were recorded over several hours to ensure equilibrium was achieved at each pressure.

Gas or gases used	Sequence for total pressures
CO ₂	Ambient to 18 bar, return to ambient
CO ₂ /N ₂	Ambient to 35 bar, return to ambient
H ₂	Ambient to 18 bar, return to ambient
CO ₂ /CH ₄	Ambient to 35 bar, return to ambient
H ₂	Ambient to 18 bar, return to ambient
CO ₂ /H ₂	Ambient to 35 bar, return to ambient

and WAXS measurements were conducted as a function of gas pressure in a series of *in situ* single gas flow experiments using pure CO₂, CH₄ or H₂ at pressures up to 1.8 MPa (18 bar). The experiments with CH₄ and H₂ were immediately followed by experiments using a dual gas flow of CO₂/CH₄ or CO₂/H₂, respectively, up to a total pressure of 3.5 MPa (35 bar). Separately, a dual gas flow experiment was conducted for CO₂/N₂ under similar conditions. In each of the dual gas flow experiments, the nominal 100 ml min⁻¹ total gas flow was distributed equally between the two gases, with corrections for the different gas constants for CO₂, N₂, CH₄ and H₂ applied automatically by the Hiden XCS control software. Measurements were made over several hours to establish equilibrium at each measurement condition. During each study both the SAXS profile and the positions of selected XRD peaks were followed as a function of total or partial CO₂ gas pressure to determine the effects of gas adsorption on the microstructure and structure of the sample. Table 1 summarizes the gas flow measurement conditions.

2.2.2. Measurements exploring critical point and supercritical CO₂ conditions. For high-pressure CO₂ sorption studies under static (non-flow) conditions, a custom-designed capillary gas pressure system was used, also detailed previously (Ilavsky *et al.*, 2018; Allen *et al.*, 2018). A small quantity of Ni-BpyMe powder was mounted in the center of a 1.5 mm diameter capillary (internal diameter = 1.3 mm) and held in place with porous glass wool plugs at each end of the capillary. The capillary was connected to a Teledyne Isco 1000D syringe pump gas system (Teledyne, Lincoln, Nebraska, USA) that enabled CO₂ pressures to be increased into the supercritical regime. In this arrangement a thermocouple was mounted through one end of the capillary and heating coils were mounted adjacent to the capillary, allowing temperature selection and calibration. The sample was activated by a gentle purge of the system with flowing CO₂, pressurizing the system to 0.5 MPa (5 bar) CO₂ under static (non-flow) conditions, followed by a second gentle purge of flowing CO₂. The system was then sealed and pressurized to the desired CO₂ pressure under static non-flow conditions. USAXS/SAXS/WAXS measurements were carried out at several sub-critical CO₂ pressure values with the sample held at 363 K (90°C). The system pressure was incremented in small intervals through the supercritical gas transition at ~ 7.3 MPa (73 bar) CO₂ to

Table 2

Pressure and temperature steps for supercritical CO₂ pressure measurements.

Key for CO₂ phases: GAS = gas, SC = supercritical, LIQ = liquid. Measurements were made over several hours to ensure equilibrium was achieved at each set point prior to measurement. (1 bar = 0.1 MPa.)

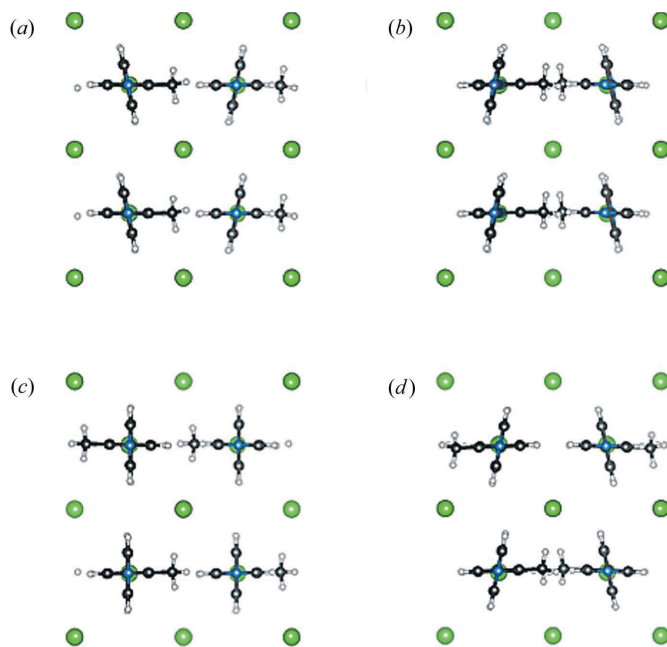
Sequence number	Pressures (bar)	Temperatures (°C)	Phase transition
1	2 to 78	90	GAS to SC
2	78	90 to 30	SC to LIQ
3	78 to 65	30	LIQ to GAS
4	65	30 to 40	GAS only
5	65 to 78	40	GAS to SC
6	78 to 65	40	SC to GAS
7	65	40 to 30	GAS only
8	65 to 78	30	GAS to LIQ
9	78	30 to 60	LIQ to SC
10	78 to 2	60	SC to GAS

7.8 MPa (78 bar) CO₂ gas pressure. Several pressures and temperatures were investigated in the supercritical CO₂ regime to explore the region around the CO₂ critical point and to examine the reversibility of changes associated with pressure and temperature variations, as well as changes associated with CO₂ phase transitions in both directions. Finally, at a sample temperature of 333 K (60°C), the pressure was reduced in increments to ambient. Table 2 summarizes the ten-step sequence of changes in pressure and temperature used to investigate microstructural and structural effects, including those associated with phase transformations among the gas, supercritical and liquid regimes during excursions around the CO₂ critical point. The USAXS/SAXS/WAXS configuration was as used for the dual gas flow studies.

2.3. DFT modeling

To gain a better understanding of the energetics of gas adsorption and the effect of gas adsorption on the unit-cell parameters of Ni-BpyMe, we turn to DFT calculations. These were conducted to help elucidate both some of the structural changes during dual gas flow adsorption and desorption and those associated with any enhanced adsorption under supercritical CO₂ conditions. In previous work (Wong-Ng *et al.*, 2021; Cockayne *et al.*, 2021), we showed that dispersion-corrected DFT methods, employing the DFT code *VASP* (Version 5.4.1; Kresse & Furthmüller, 1996*a,b*), reproduced the structure of empty Ni-BpyMe. A key step was to represent the methylpyridine ring orientational disorder by an ensemble of 1 × 2 × 2 supercell structures, each with different orientational ordering. As shown in Fig. 3, prepared using the *VESTA* visualization software package (Momma & Izumi, 2008), a number of characteristic local orientational ordering patterns exist for Ni-BpyMe. As favorable positions and energetics of adsorbate species depend on local orientational ordering, we performed multiple calculations on differing representative supercells.

The procedure here was the same as that used by Cockayne (2019). A single adsorbate molecule per asymmetric unit of the supercell was added, the structure fully relaxed, then another adsorbate molecule added and so on. The space


Figure 3

Selected orientational ordering patterns of the methylpyridine rings in Ni-BpyMe, viewed down the *z* axis. Ni atoms are shown in green, C dark gray, N blue and H white.

groups chosen for the adsorbate supercells maintained the orthorhombic symmetry but were also subgroups of the empty supercell space group with four asymmetric units per supercell. The asymmetric units were designed to coincide with the natural channels along the *x* direction bounded by ligands in the *y* direction and wavy Ni(CN)₂ planes in the *z* direction. As the *Z* = 8 supercell contains eight BpyMe ligands, the adsorbate concentrations studied were multiples of 0.5 per ligand. Unfortunately, no supercell with the local environments shown in Fig. 3(*d*) satisfied the desired constraints, so we used three supercell structures, namely each of the lowest-energy structures of Figs. 3(*a*), 3(*b*) and 3(*c*) that satisfied the constraints, and then averaged the results.

3. Results and discussion

In the sub-sections that follow, results are presented in each case for the observed variations in XRD peak lattice spacing *d* with gas adsorption and desorption, as well as the associated observed microstructural changes. We then discuss some insights that can be gained from DFT calculations and predictions of the Ni-BpyMe structural response to the gas and pressure conditions applied. Theoretical structural considerations that the *x* direction should be the most flexible due to the wavy Ni(CN)₂ planes (Cockayne *et al.*, 2021) are consistent with diffraction results and DFT calculations in this work that imply that the *a* lattice parameter changes the most upon gas sorption. In terms of the reciprocal lattice, the main structural response to gas sorption effects is thus reflected in changes in peak position for *h*00 and *h*-small-small XRD peaks, with little or no effect for other XRD peaks. Therefore,

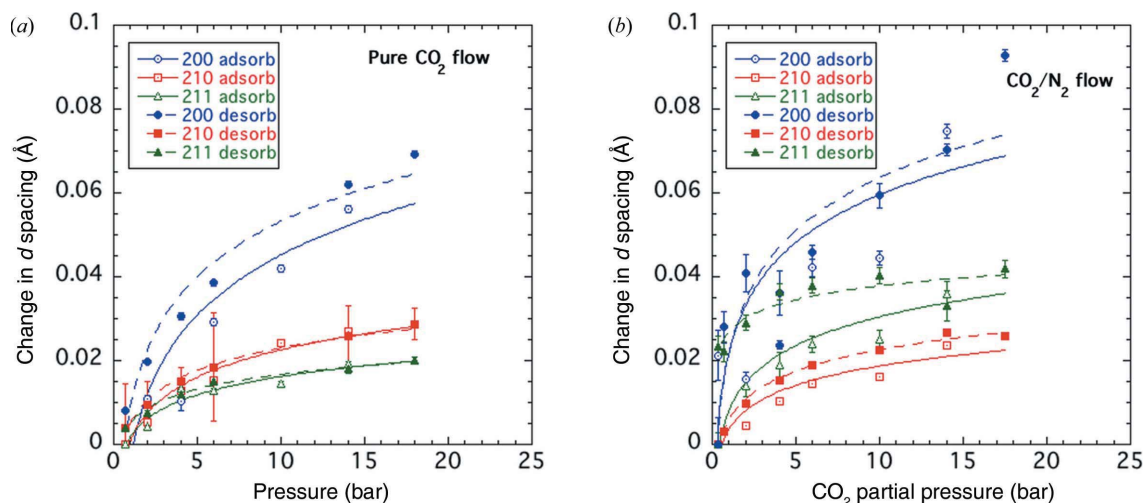


Figure 4

Changes in d spacing for the 200, 210 and 211 XRD peaks during adsorption and desorption of (a) pure CO_2 under single gas flow conditions and (b) CO_2/N_2 under dual gas flow conditions. Here and in Figs. 5 and 6, vertical bars represent the computed standard uncertainties of the Lorentzian peak least-squares fit d -spacing results.

we have selected three of the former as our primary measures of structural response to gas adsorption and desorption.

3.1. Effects on NiBpyMe under single and dual gas flow conditions

Despite this system not exhibiting major swelling behavior or structural transformations during gas sorption, some XRD peaks (notably 200, 201, 210, 211 and 202) show modest, and mainly reversible, changes during CO_2 adsorption and desorption (and to some extent for other gases), while others do not show such changes (notably 001, 011 and 002). DFT calculations have provided some insights as to why this is so, hence providing a foundation from which to develop further insights with regard to CH_4 and H_2 adsorption, especially when combined with CO_2 adsorption, as well as for CO_2 sorption phenomena exhibited in the supercritical CO_2 regime for Ni-BpyMe. To explore the structural response to gas adsorption and desorption, changes in the 200, 210 and 211 XRD peaks have been followed as a function of gas pressure in the sections that follow.

3.1.1. CO_2 and CO_2/N_2 . As an example of the combined USAXS/SAXS/WAXS data sets obtained, Fig. 2 presents reduced and calibrated USAXS/SAXS and SAXS/WAXS (XRD) data for CO_2 adsorption and desorption under gas flow conditions, including an expansion of the XRD data for the q range that includes the 200, 210 and 211 XRD peaks. As with all the subcritical gas flow adsorption studies, the observed microstructural changes during adsorption and desorption are subtle [Fig. 2(a)], except for a modest increase in nanoscale pore component and also the flat scattering background apparent at higher SAXS q values when pressurized gas is present in the pores. Combined USAXS/SAXS curves are shown in the supporting information (Figs. S3, S4 and S5) for all of the single and dual gas flow studies. Given the relatively subtle changes observed here, we defer discussion of microstructural changes to the supercritical CO_2 studies presented later.

Some XRD peaks do exhibit largely reversible position shifts during CO_2 adsorption and desorption [Fig. 2(b)]. Fig. 4 presents data for the changes in d spacing of the XRD peaks 200, 210 and 211, as measured during adsorption and desorption. At risk of over-simplification, the lattice expansion of each XRD peak approximates in shape to the reversible isotherm curve (Fig. S1) when measured against total CO_2 or partial CO_2 gas pressure for pure gas or dual gas flow, respectively, with the order of sensitivity being $200 > 210 > 211$ for pure CO_2 , but $200 > 211 > 210$ for dual gas flow. However, note that the CO_2/N_2 dual gas flow measurements were made separately from the pure CO_2 flow experiments, with the sample exposed to ambient environment between the two sets of measurements.

3.1.2. CH_4 and CO_2/CH_4 . Fig. 5 presents the changes in d spacing for the fitted 200, 210 and 211 XRD peaks with pure CH_4 gas flow and with CO_2 or CH_4 partial pressure in the case of CO_2/CH_4 dual gas flow. In pure CH_4 gas flow, the 200 XRD peak d spacing expands and contracts approximately in line with the CH_4 adsorption isotherm curve (see Fig. S1), although the d -spacing changes are smaller than with pure CO_2 flow. The change in the 210 d spacing shows some hint of the adsorption/desorption curve but at a very much reduced level, while the 211 d spacing shows virtually no change during CH_4 adsorption and desorption. In this context, it is worth comparing the size of the CH_4 molecule (3.8 Å) with the absolute d spacings associated with the 200 (~6.4 Å), 210 (~4.8 Å) and 211 (~4.4 Å) XRD peaks. Clearly, CH_4 molecules are more easily accommodated within the 200 d spacing than either of the 210 or 211 d spacings. For the CO_2/CH_4 dual gas flow measurements, the shape of the CO_2 isotherm as a function of CO_2 partial pressure is restored in the d -spacing variation to a great extent, although with more stochasticity exhibited than for CO_2/N_2 , especially for 210. The d -spacing variation, as a function of CO_2 partial pressure, follows the order $200 > 210 > 211$, the same as that for pure CH_4 and pure CO_2 gas flow, but different from CO_2/N_2 dual gas flow. Also, the variations are slightly smaller than for pure CO_2 flow.

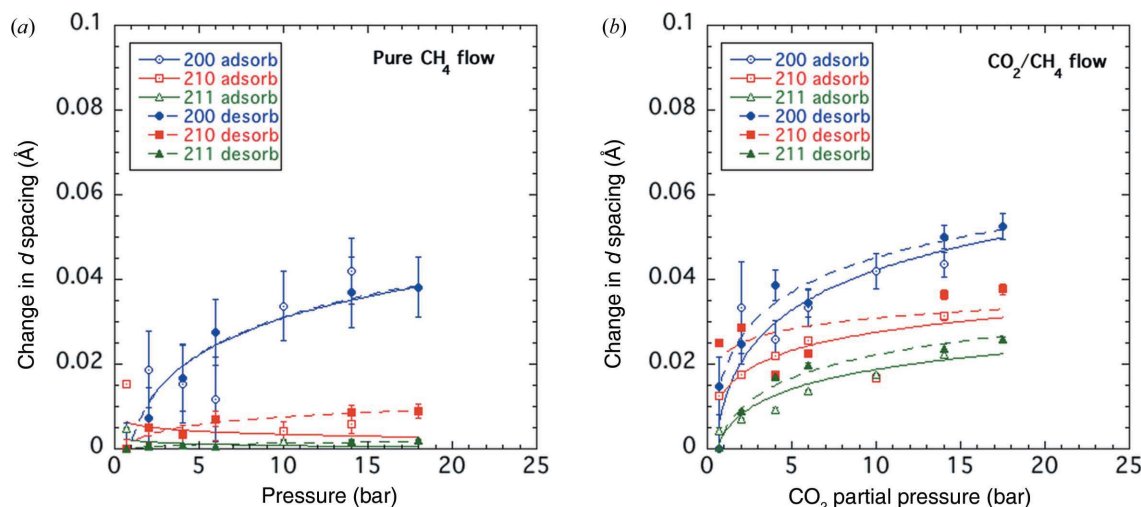


Figure 5 Changes in d spacing for the 200, 210 and 211 XRD peaks during adsorption and desorption of (a) pure CH_4 under single gas flow conditions and (b) CO_2/CH_4 under dual gas flow conditions.

3.1.3. H_2 and CO_2/H_2 . Changes in d spacing for the fitted 200, 210 and 211 XRD peaks with pure H_2 gas flow and with CO_2 or H_2 partial pressure in the case of CO_2/H_2 dual gas flow are presented in Fig. 6. For pure H_2 gas flow, Fig. 6(a) indicates that there is no significant systematic change in d spacing for pressures up to 18 bar. On switching to CO_2/H_2 dual gas flow, there is some significant increase in d spacing due to CO_2/H_2 adsorption, but the shape of the variation plotted against CO_2 (or H_2) partial pressure deviates somewhat from that of the adsorption isotherm. This is especially true for 200 but is also the case to some extent for 210 and 211. However, the corresponding decrease in d spacing during desorption follows the isotherm curve without such significant deviation. Measured against CO_2 partial pressure, the changes in d spacing are comparable to or slightly less than those measured for pure CO_2 adsorption, with the magnitude of variation in the order $200 > 211 > 210$, as found for pure CO_2 or dual gas

CO_2/N_2 . It is surprising not to observe measurable changes in XRD d spacings for pure H_2 adsorption, given that the size of the molecule ($< 3 \text{ \AA}$) is significantly smaller than the d spacings associated with these peaks. Although no H_2 isotherm data are available for Ni-BpyMe, it seems likely that many more guest H_2 molecules need be adsorbed than for the other gases to exhibit measurable swelling of the d spacings. This point may be connected with the role played by H atoms within the solid matrix (Wong-Ng *et al.*, 2021; Cockayne *et al.*, 2021) and suggests that much higher gas flow pressures than used here would be required to achieve a measurable effect.

3.2. Effects on NiBpyMe of exploring the CO_2 phase diagram around the critical point

The sequence steps numbered 1 to 10 in Table 2 are considered in the following pairs in the sub-sections below:

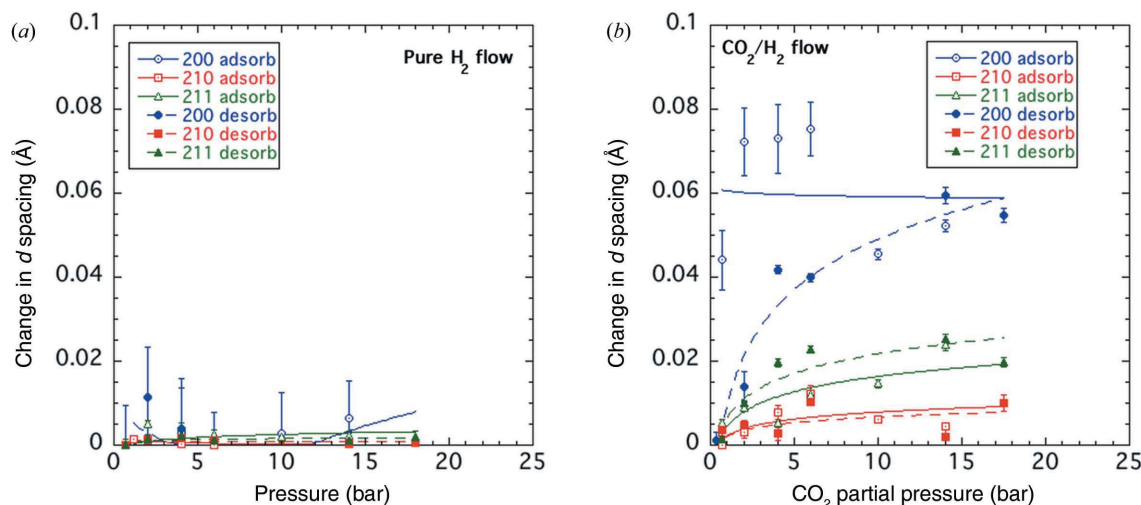


Figure 6 Changes in d spacing for the 200, 210 and 211 XRD peaks during adsorption and desorption of (a) pure H_2 under single gas flow conditions and (b) CO_2/H_2 under dual gas flow conditions.

1 and 10, 2 and 9, 3 and 8, 4 and 7, 5 and 6. Thus, apart from the different initial and final temperatures, the second step listed in each pair is the reverse of the first step listed. In this way, the reversible nature of the changes associated with each step in the sequence can be evaluated, as well as the reversibility of the steps intervening between the end of the first step of each pair and the start of the second (reverse) step. For each pair of steps in the sequence, structural changes are considered primarily with regard to changes in the d spacing of the 200, 210 and 211 XRD peaks. We then go on to consider the significant effects on the microstructure, as indicated by changes in the measured USAXS/SAXS data, associated changes in the scattering contrast factor and changes in the derived MaxEnt pore volume fraction size distributions.

3.2.1. Effects on 200, 210 and 211 XRD d spacings. Before proceeding, we note that, just as in the gas flow studies at subcritical pressures, many Ni-BpyMe XRD peaks show no obvious sorption-induced changes in position or associated d spacings. This is due to the differing degrees of freedom allowable for different parts of the unit cell. To follow the changes in d spacing through the sequence of pressure and temperature steps, reference should be made to both Table 2 and Fig. 7(a). By presenting data for the changing d spacings of the three XRD peaks as shown in Figs. 7(b) to 7(f), it is possible to evaluate which of the observed changes are reversible and which are irreversible, at least to some degree.

All three XRD peak d spacings vary similarly during the various steps, with the magnitudes of response in the order $200 > 210 > 211$, similar to the situation for most of the subcritical gas flow studies. It is also clear that *changes* in d spacing during the first and last steps (1 and 10) appear reversible for all three peaks. However, the *absolute* d spacing values are larger during the final desorption step at 60°C than during the initial adsorption step at 90°C [Fig. 7(b)]. It is also of interest that all the d spacings increase slightly both on entering the supercritical regime (step 1) and on leaving it (step 10) from/to the gas regime. In this connection, it is important to note the direction of each step in Figs. 7(b) to 7(f). For example, the track of step 1 in Fig. 7(b) is left to right, while that of step 10 is right to left.

On following the steps through the graphs of Fig. 7, after Fig. 7(b) showing the initial adsorption step, it is observed that all three d spacings increase slightly once again on cooling from the supercritical to liquid CO₂ regime [Fig. 7(c)], increase continuously on partial depressurization back into the gas regime [Fig. 7(d)], continue to increase slightly on reheating wholly in the gas regime [Fig. 7(e)] and barely change on repressurization into the supercritical regime [Fig. 7(f)]. On reversing these steps, the d spacings increase continuously and significantly on partial depressurization back into the gas regime [Fig. 7(f)], continue to increase even more significantly on cooling wholly within the gas phase [Fig. 7(e)], do not change significantly on repressurization into the liquid regime [Fig. 7(d)], increase once more on re-entering the supercritical regime during heating [Fig. 7(c)], and increase further on transition back to the gas regime, before finally decreasing during final desorption [Fig. 7(b)]. While the increases in d

spacing during steps 1 and 2 and 9 and 10 occur at or close to the phase boundaries between supercritical CO₂ and either the gas or liquid CO₂ phases, the increases elsewhere occur more continuously through the various conditions sampled during steps 3 to 8. The reasons underlying the irreversible changes observed must relate to the effects of the phase transitions on CO₂ sorption in the Ni-BpyMe matrix, as well as to the presence of supercritical or liquid CO₂ in void spaces.

3.2.2. Effects of supercritical CO₂ conditions on Ni-BpyMe microstructure. To interpret the USAXS/SAXS data and associated Ni-BpyMe microstructure during supercritical CO₂ adsorption studies, we need to consider the variation in scattering contrast factor between the CO₂ fluid in the pore and void spaces and the CO₂-loaded Ni-BpyMe solid matrix. Generally, the solid matrix has a higher X-ray scattering length or form factor density than the pore fluid, but two effects need to be considered: an increase in CO₂ density with respect to ambient conditions increases the CO₂ X-ray scattering length density in the void spaces, reducing the scattering contrast factor with the matrix, while adsorbed CO₂ within the solid Ni-BpyMe matrix increases the solid matrix density and hence also the scattering contrast factor with the pore fluid. A trade-off between these two effects determines the effective scattering contrast factor which, in turn, determines the absolute pore and void volume fractions obtained from a given USAXS/SAXS profile and interpretative model – here MaxEnt size distribution analysis where globular pores have been assumed for simplicity. Note that smaller scattering contrast factors result in greater volume fractions of scattering pores or voids.

Available information on the density of CO₂ under conditions of interest (Span & Wagner, 1996) and previously established information on the composition, structure and skeletal density of Ni-BpyMe (assumed skeletal density 1.23 g cm⁻³), its CO₂ sorption characteristics (Wong-Ng *et al.*, 2016, 2021), and published X-ray scattering length or form factor information for all atomic species present (Chantler *et al.*, 2005) have been combined in Table S1. This summarizes calculations of the effective X-ray scattering contrast factor applicable to scattering from pores and voids in Ni-BpyMe under selected conditions of temperature and CO₂ pressure. In Fig. S6, the calculated X-ray scattering contrast factor variations are plotted for all sequence steps of the supercritical CO₂ gas studies of Ni-BpyMe, together with the trajectory followed on the CO₂ phase diagram [reprinted from Fig. 7(a)] for reference. Some significant extrapolation has been made in estimating the CO₂ adsorption (mmol g⁻¹ CO₂/Ni-BpyMe) under conditions where measured results are unavailable. Nevertheless, we consider that the scattering contrast factor values deduced provide the basis for a working model for evaluating microstructure changes in the Ni-BpyMe sorbent/sorbate system during these supercritical CO₂ sorption studies. Using the scattering contrast factor information, MaxEnt void volume fraction size distributions have been derived for each condition studied and then interrogated to evaluate the fine (nanoscale) and coarse (mesoscale) porosities, together with the associated mean pore diameters. The USAXS/SAXS data

sets from which the MaxEnt size distributions have been derived and the MaxEnt size distributions themselves, together with the fine and coarse porosities and corresponding mean pore diameters, are all available in the supporting information, Figs. S7–S16. None of the mean pore diameters,

of either the fine or coarser pores, vary greatly during any part of the supercritical CO₂ studies. Thus, our discussion will primarily concentrate on the porosity variations.

As with the structural variations measured by changes in XRD *d* spacings, the microstructural variations are considered

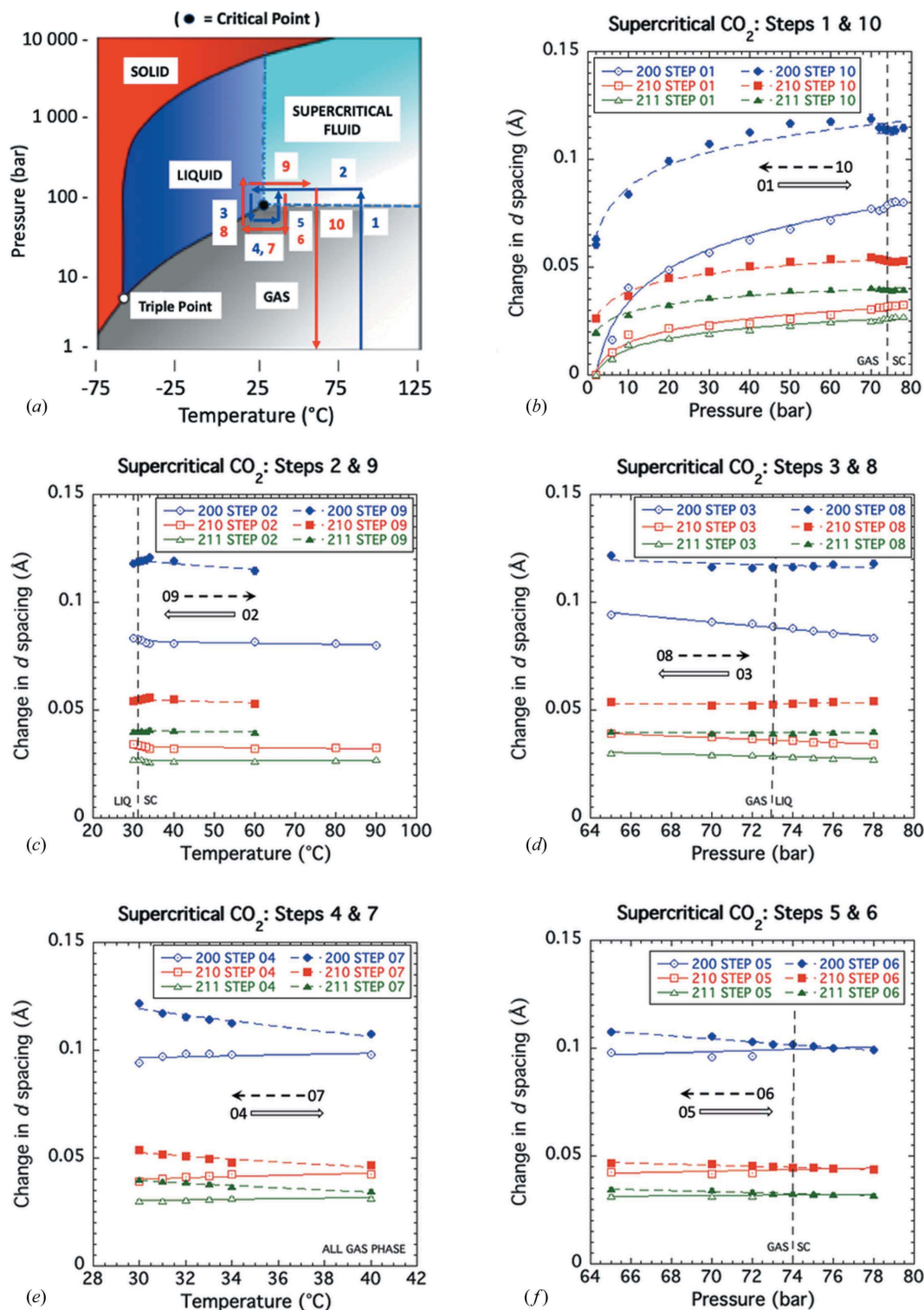


Figure 7 Structural changes in Ni-BpyMe during supercritical CO₂ sorption studies. (a) A schematic diagram showing the sequence steps in relation to the CO₂ phase diagram. (b)–(f) The 200, 210 and 211 *d* spacings plotted versus pressure or temperature for (b) steps 1 and 10, (c) steps 2 and 9, (d) steps 3 and 8, (e) steps 4 and 7, and (f) steps 5 and 6. Computed peak fit uncertainties are smaller than the sizes of the symbols.

with reference to the ten-step sequence of temperature and pressure variation around the supercritical point on the CO₂ phase diagram. We start with Fig. 8, which presents the MaxEnt pore volume fraction size distributions associated both with the initial and final pressure-induced CO₂ phase transitions between the gas and supercritical regimes, steps 1 and 10, and with the temperature-induced CO₂ phase transitions between the supercritical and liquid regimes, steps 2 and 9. The pore volume fraction size distributions can be considered to consist of two main pore populations. There is a very fine nanoscale pore population, taken as the first prominent peak in the size distribution with a maximum diameter ranging from 25 to 40 Å. There is then a population of coarse mesoscale pores ranging over many length scales from less than 100 Å up to ~10 000 Å. Larger voids between the powder grains were excluded from the analysis as discussed previously.

The MaxEnt size distributions presented in Figs. 8(a) and 8(b) show that, while the changes in the fine pore population during both the initial adsorption step into the supercritical CO₂ regime and the final desorption step are largely reversible, the fine pores have clearly become (irreversibly) more prominent with respect to the coarser porosity during the overall ten-step sequence. Meanwhile, Figs. 8(c) and 8(d) show a reversible, but much more significant, increase in the relative prominence of the fine porosity when the system is in the liquid CO₂ regime. This *relative* enhancement of the fine

porosity with respect to the coarser pore population is far more significant than can be accounted for by changes in the scattering contrast factor on entering the liquid CO₂ regime – see Table S1 and Fig. S6. Unlike the case for CO₂ in either the gas or supercritical states, CO₂ in the liquid state has an associated surface tension and capillarity that can lead to ‘beading’, with some nanoscale pores filled with CO₂ and others vacant. These regions will have higher scattering contrasts with respect to each other, and any vacant nanoscale pores will scatter more strongly with respect to the solid sorbent. We tentatively attribute this as the explanation for the enhanced apparent relative prominence of the nanoscale pores. We also note that this implied redistribution of CO₂ within the fine nanoscale pores in the liquid state may not be as fully reversible as other such changes observed for the system.

Fig. 9 summarizes porosity information for the initial and final pressure steps, 1 and 10, into and out of the supercritical CO₂ regime, and also for the adjacent initial cooling and final heating steps, 2 and 9, into and out of the liquid CO₂ regime. Fig. 9(a) shows that, while the changes in fine porosity for step 1 are essentially reversed in step 10, the absolute level of fine porosity during step 10 is greater than that for step 1, confirming that there has been some irreversible increase during the intervening steps. The corresponding coarse porosity variations shown in Fig. 9(b), on the other hand, do not show any significant irreversibility. This is consistent with

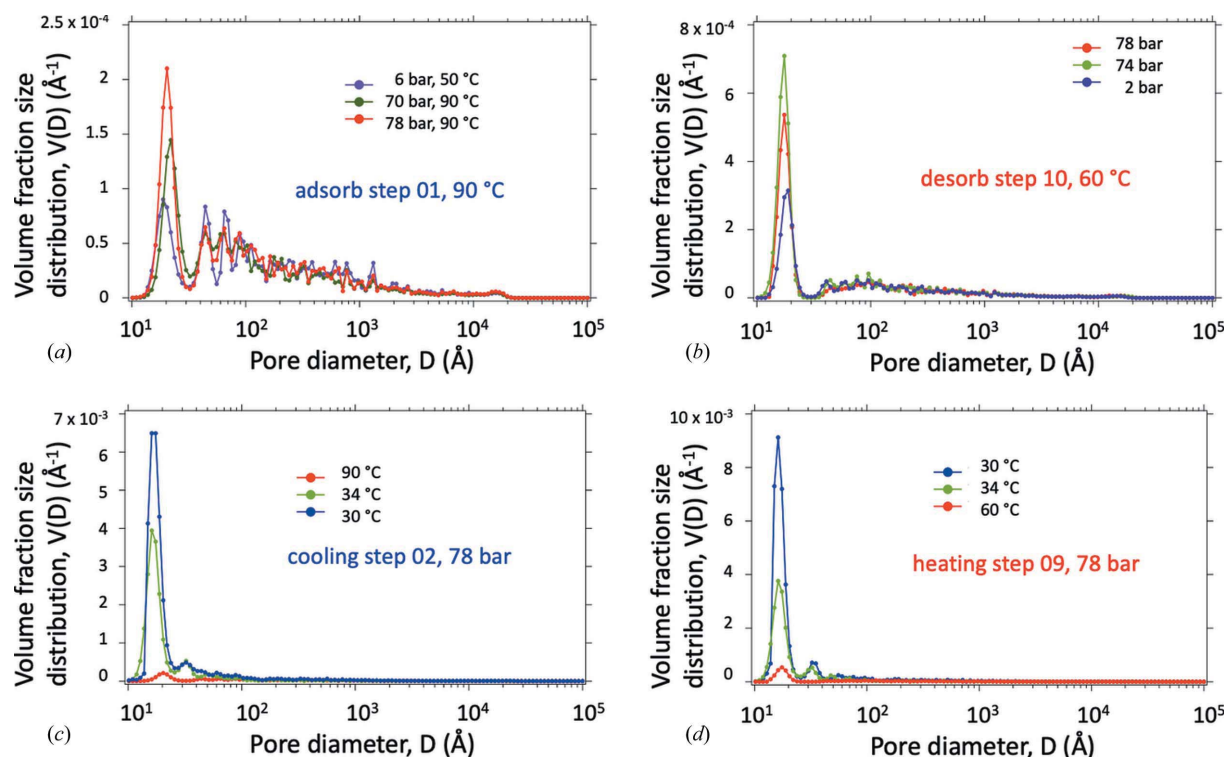


Figure 8 MaxEnt volume fraction size distributions, $V(D)$ versus diameter D , for (a) step 1, (b) step 10, (c) step 2 and (d) step 9. Note that, because of the logarithmic diameter scale, these plots are heavily weighted in favor of fine pores, and thus the coarse porosity, integrated over its own wide range of length scales, is far more significant than is apparent in these figures. Features larger than 10 000 Å, attributed to gaps between the powder grains, are excluded from further analysis. Uncertainties associated with MaxEnt size distribution calculations are complex to estimate but are indicated by visible random fluctuations in $V(D)$.

the significantly greater fine porosity for step 10, shown in Fig. 8(b), while other parameters remain comparable.

Also shown in Figs. 9(c) and 9(d) are the changes in fine and coarse porosities on cooling/heating to/from the liquid regime from/to the supercritical regime, steps 2 and 9. While the changes of step 2 are largely reversed in step 9, there is an order of magnitude increase in fine nanoscale porosity in the liquid regime compared with the supercritical CO₂ regime. As already discussed above, this is greater than accounted for using the predicted decrease in scattering contrast factor in the liquid regime to calculate volume fractions from the measured scattering intensities. Other parameters, such as the coarse porosity, do not vary so significantly, suggesting that the predicted scattering contrast factor variation is a reasonable estimate.

In Figs. 10(a) and 10(b), summarizing the effects of steps 3 and 8, both the fine and coarse porosities decrease/increase by a factor of ~2.5 on exiting/entering the liquid regime through desorption or adsorption at 30°C. It seems possible that the predicted increase in scattering contrast factor on moving from the liquid regime to the gas regime through a partial depressurization may be over-compensating in this case, except for the fact that this trend continues for the fine

nanoscale porosity on heating/cooling solely in the gas regime, steps 4 and 7, as indicated in Fig. 10(c). There is some reversible recovery in the fine porosity during steps 5 and 6, heating/cooling into/out of the supercritical regime once more, as indicated in Fig. 10(e). Meanwhile, the coarse porosity does not change significantly throughout steps 4 to 7 [Figs. 10(d) and 10(f)]. The microstructure, as measured by pore size distribution in the supercritical regime at 40°C and 78 bar CO₂ pressure (Fig. S16), relates to cases under similar pressures in the supercritical regime at 60 or 90°C (Fig. 8), but the fine porosity is higher at 40°C and the coarse porosity slightly lower.

Unlike the structural changes based on XRD peak *d*-spacing determinations, discussed earlier, most of the microstructural changes observed, even the somewhat significant changes in the liquid regime, are largely reversible over the ten-step sequence explored. The greater prominence of the fine nanoscale porosity in the final desorption step, compared with the initial adsorption step, may also be attributable in part to the lower temperature: 60°C for desorption compared with 90°C for adsorption. Nevertheless, it is interesting how the more irreversible structural changes relate to the microstructural changes during the sequence, especially

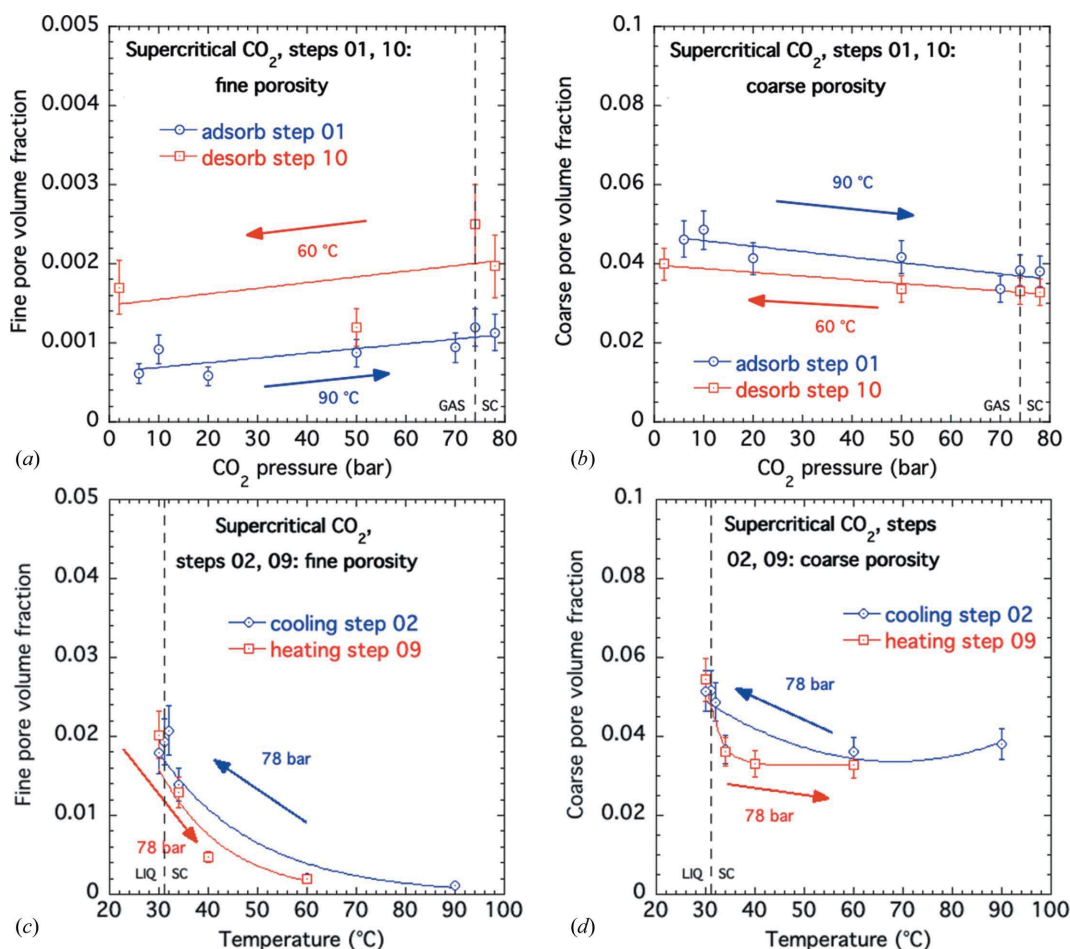
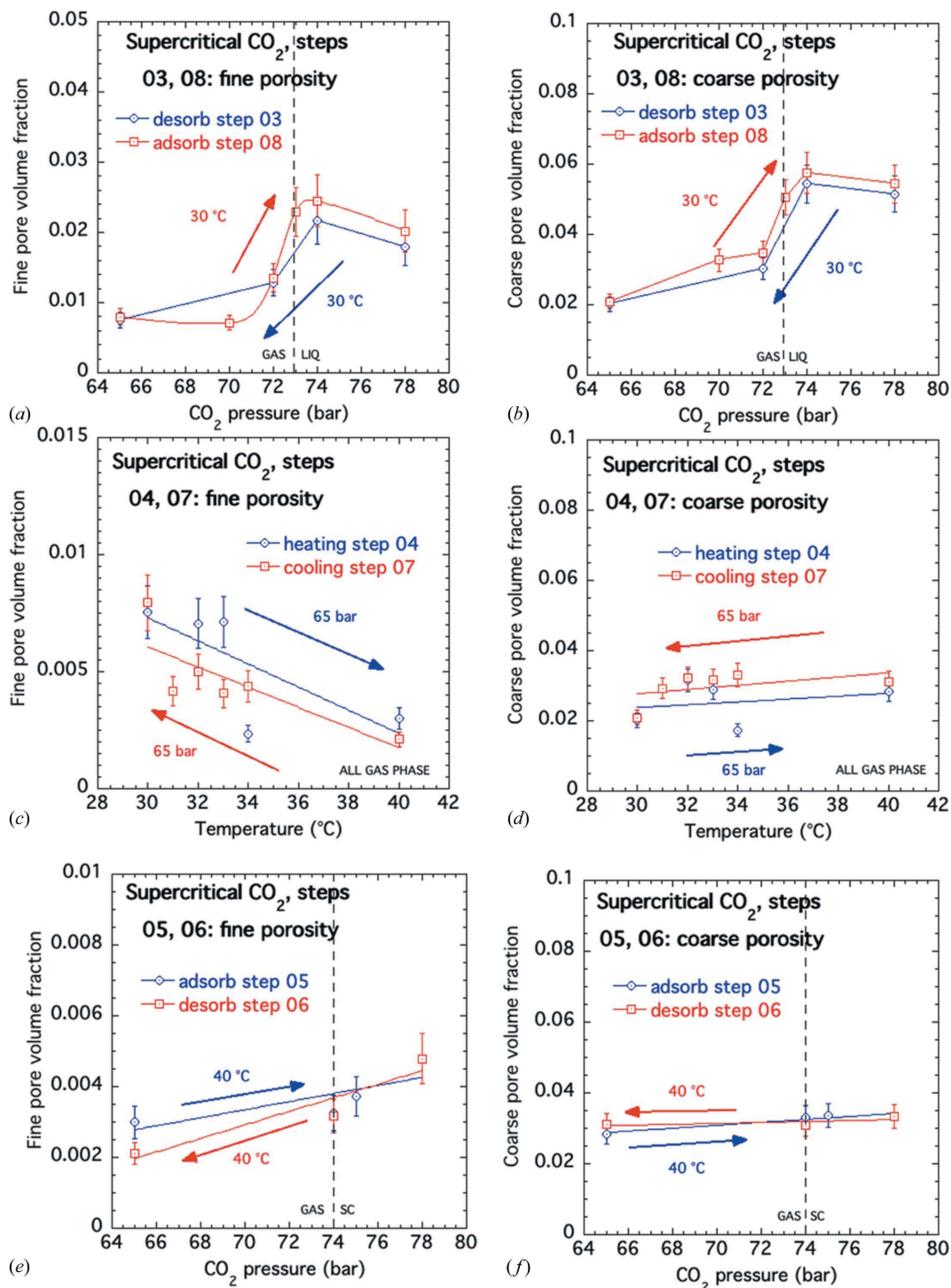


Figure 9 Volume fraction (porosity) variations for fine and coarse pores, determined from MaxEnt size distribution analysis of USAXS/SAXS data sets, during steps 1 and 10, (a) fine and (b) coarse porosities, and steps 2 and 9, (c) fine and (d) coarse porosities. Here and in Fig. 10, arrows indicate the directions in time of each numbered step, and the vertical bars are estimated standard uncertainties based on multiple similar studies using the APS USAXS facility.


Figure 10

Volume fraction (porosity) variations for fine and coarse pores, determined from MaxEnt size distribution analysis of USAXS/SAXS data sets, during steps 3 and 8, (a) fine and (b) coarse porosities; steps 4 and 7, (c) fine and (d) coarse porosities; and steps 5 and 6, (e) fine and (f) coarse porosities.

given the recognized role of supercritical and liquid CO₂ to act as a solvent in MOF systems such as Ni-BpyMe.

3.3. DFT results

In Fig. 11, prepared using the *VMD* visualization software (Humphrey *et al.*, 1996), we show the available internal pore space for CO₂ molecules in a representative supercell configuration. The most favorable locations for adsorbate molecules

in Ni-BpyMe lie primarily within the $y = 0$ plane along the 101 orientation (dimension ~ 17 Å) in the unit cell, with a ‘waviness’ reflecting the relative orientations of neighboring ligands.

Fig. 12 indicates how the Ni-BpyMe structure ‘breathes’ on CO₂ and CH₄ adsorption/desorption. It presents the configuration- and symmetry-averaged valence charge density in the $y = 0$ plane for the supercell as a function of CH₄ and CO₂

concentration. The results are simpler for CH₄ than for CO₂. At $N = 1$ CH₄ per BpyMe ligand, favorable dispersion interactions place the CH₄ molecule between BpyMe ligands at $x = 0.25$, above a trough in the Ni(CN)₂ sheet, but not over any specific atom in this sheet. For $N = 2$, there is a second Ni site appearing as 0.5 occupancy of two split positions at about $x = 0$. At $N = 3$, the split separation is sufficient to allow full occupancy. Note that some movement of the CH₄ molecule off the $y = 0$ plane occurs to allow for more favorable intermolecular distances, especially at high concentration.

The CO₂ charge density plots (Fig. 12, right-hand column) are dominated by the O atoms. For CO₂ at $N = 0.5$, the most favored CO₂ position is roughly similar to that of the most favorable CH₄ position at low concentration, with one O of the CO₂ molecule at about $x = 0.25$. Three peaks are seen for each CO₂ in Fig. 12, corresponding to randomized mirror-image positions for the other O of the CO₂ molecule. The tilted CO₂ orientation is similar to that calculated for CO₂ adsorption on open metal sites of various MOFs, but interestingly, the CO₂ is not ‘pinned’ to an open metal site in this system. For $N = 1$, rather than full occupancy of the most favored position, there is a mixture of the most favored CO₂ position and a secondary one. Now five density peaks are visible in Fig. 12, corresponding to a statistical mixture of the O positions of an interacting pair of CO₂ in one of two mirror-image configurations. Given the significantly higher temperature to which CO₂ is solid at atmospheric pressure compared with CH₄, it is not surprising that interactions between CO₂ adsorbate molecules are more important. For $N = 2$, pairs of

CO₂ molecules are essentially fully occupied. For $N = 3$, the description of the CO₂ molecules in terms of favored positions breaks down, as there are different configurations of the CO₂ for the different local ligand methylpyridine units, and we note that the displacements of CO₂ O atoms off the $y = 0$ plane become significant. The binding sites for N₂ and for H₂ at low concentrations, $N = 0.5$, are similar to those for CH₄; higher concentrations were not explored.

In Table 3, the DFT results for the change in the unit cell of Ni-BpyMe and the incremental energy of adding additional adsorbate molecules are shown. The results show a weak form of ‘breathing’ behavior: contraction of the unit cell up to $N = 2$ and then expansion at $N = 3$. The binding energies monotonically become less favorable as N increases and are similar for CH₄ and CO₂. The predicted changes in the unit-cell shape (with respect to the starting cell parameters a_0 , b_0 and c_0) are different for CH₄ and CO₂, with CH₄ having a lower a/a_0 ratio

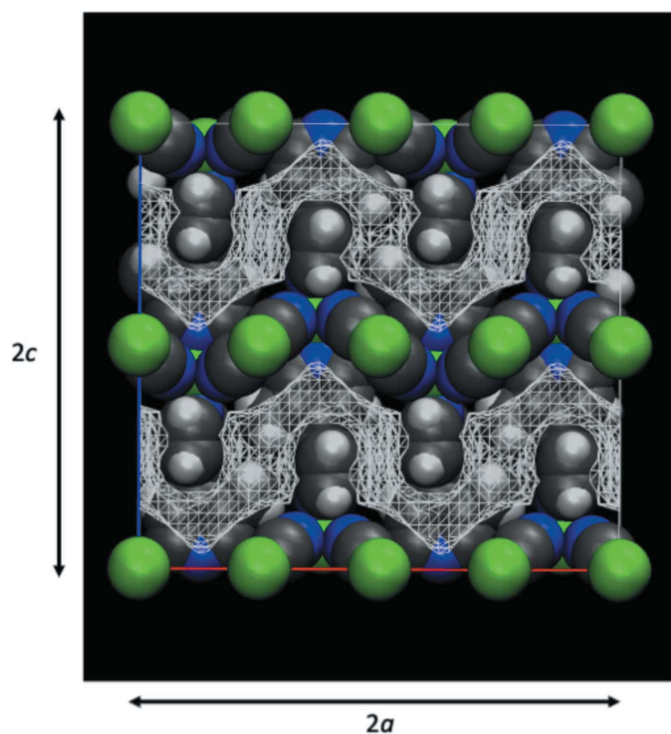


Figure 11
The available pore space for CO₂ molecules in a representative supercell configuration. Ni atoms are shown in green, C in dark gray, N in blue and H in light gray, and the mesh represents the available internal pore space.

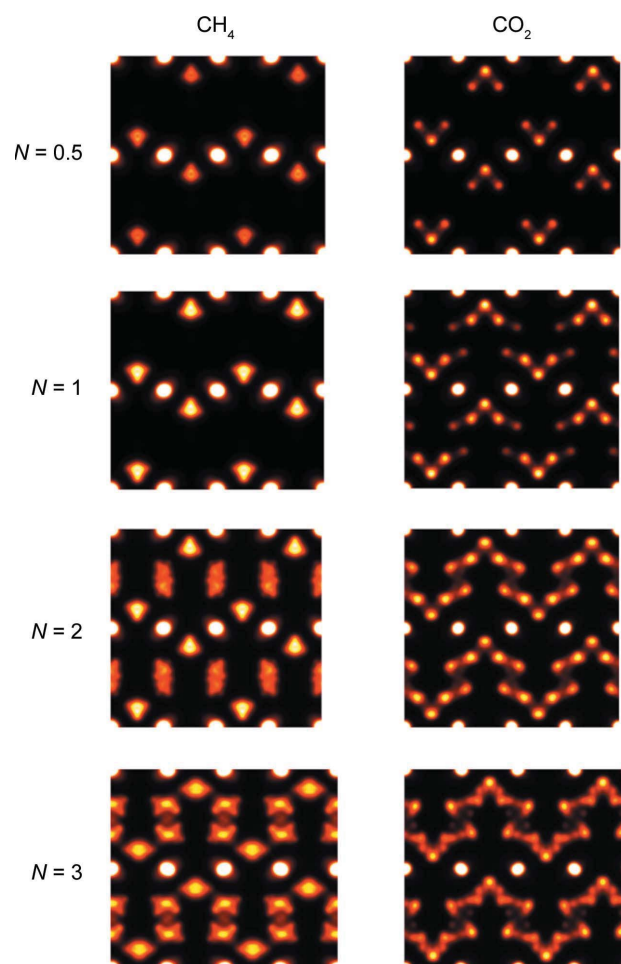


Figure 12
‘Heat maps’ showing the configuration- and symmetry-averaged valence electronic density in the xz plane at $y = 0$ as a function of adsorbate concentration per ligand N for CH₄ and CO₂. The area shown corresponds to Fig. 11; the horizontal coordinate in the figures runs from $x = 0$ to $x = 2$ and the vertical coordinate runs from $z = 0$ to $z = 2$, *i.e.* each plot is approximately 25.2 Å ($2a_0$) horizontal by 22.6 Å ($2c_0$) vertical. The calculated breathing of the structure is shown to scale and is most noticeable in the change of the horizontal lattice parameter a for $N = 3$.

Table 3

The DFT-calculated relative change in unit-cell parameters and incremental change in binding energy, $\Delta U_B/\Delta N$, for CH₄ and CO₂ in Ni-BpyMe as a function of the number N of adsorbate molecules per BpyMe ligand.

Note there is one ligand per Ni-BpyMe formula unit, so N = molecules of gas per molecule of Ni-BpyMe.

Species	N	a/a_0	b/b_0	c/c_0	$\Delta U_B/\Delta N$ (eV)
CH ₄	1	0.9851	1.0017	0.9987	-0.47
CH ₄	2	0.9734	0.9987	0.9972	-0.41
CH ₄	3	1.0237	0.9975	1.0014	-0.28
CO ₂	1	0.9921	0.9941	1.0002	-0.40
CO ₂	2	0.9902	0.9931	0.9995	-0.38
CO ₂	3	1.0470	1.0097	1.0011	-0.21

at all concentrations. In all cases, the a parameter is the most flexible and c is the least flexible.

While adsorbate molecules are predicted to shrink the unit cell at low concentrations, the experimental results correspond to an expansion. The reason for this discrepancy is the inherent neglect of temperature in the DFT calculations. Thermal motion of the sorbate molecules, not included in the DFT relaxations, would tend to expand the structure and render quantitative comparisons between experiment and theory beyond the scope of this paper. The DFT results do agree with experiment in the relative stiffness of the unit-cell parameters. For example, the fact that little or no change is observed in the 002 peak corresponds to the DFT stiffness of the c parameter. While the results for $N = 3$ show several percent expansion in the a parameter, none of the experimental results show so large a change. We conclude that $N < 3$ in the ‘fully loaded’ experimental results. The fact that the calculations show favorable binding energy at $N = 3$ does not contradict experiment, again because the binding energy results neglect thermal motion which tends to make binding less favorable. Finally, with the observation of adsorbate molecules going off the $y = 0$ axis at higher adsorbate concentrations, we can speculate that experimental observations of irreversibility could be due to adsorbate molecules getting ‘trapped’ between ligands at off-axis positions. Another possible explanation of irreversibility could be an irreversible change in the average concentration of different local methylpyridine orientational patterns (Fig. 3).

All structural files used to obtain sorbate positions are included in the supporting information as a zipped archive, which includes a README file for guidance.

4. Summary and conclusions

In this paper, we have investigated two aspects of gas adsorption in a previously characterized PICNIC MOF material, and we have indicated the range of structural and microstructural measurements that, when combined with DFT modeling, can lead to new insights into how such systems can be designed to optimize various gas adsorption behaviors. In particular, gas flow studies, along the lines presented here, can complement the more conventional static Sieverts-type gas

sorption studies where the sorbent is measured under specified gas pressure environments once equilibrium is achieved. Whereas some ambiguity can occur in dual gas Sieverts experiments, especially during desorption if the sample selectively desorbs one gas more than the other, in dual gas flow experiments the gas environment external to the sample is always that defined by the flow and partial pressure conditions – a situation that is usually more realistic for potential applications.

In the case of Ni-BpyMe CH₄ adsorption, the smaller change along the a axis (see the 200 XRD peak in Fig. 5) compared with the case for CO₂ is consistent with both the slightly reduced CH₄ adsorption (Fig. S1) and the DFT calculations. The latter also suggests less of an effect, even relatively, in the b and c directions than for CO₂, as is actually observed for the 210 and 211 peaks in Fig. 5. While we do not have complete data or full DFT results in the case of H₂ or N₂, it seems likely that there is less gas adsorption in either case (confirmed in Fig. S1 for N₂), and more adsorbed H₂ or N₂ molecules would be needed to show a significant change along the a axis or in the lattice spacings of the 200, 210 and 211 XRD peaks. Nevertheless, with the relatively low numbers of gas molecules adsorbed, as indicated by the isotherm measurements, the DFT calculations suggest that adsorption and desorption are reversible, with few microstructural effects observed. The system response is largely determined by adsorption of CO₂ molecules, which have the greatest effect on the Ni-BpyMe structure at a given CO₂ partial pressure.

Under supercritical CO₂ conditions, some changes in the XRD lattice spacings are observed, and DFT calculations predict possible lattice contraction and expansion depending on the conditions (without allowing for temperature). Interestingly, Fig. 7(b) indicates a slight lattice expansion on first entering the supercritical regime, but also an expansion on final desorption back to the gas state (*i.e.* some contraction in the lattice in the supercritical regime at the end of the experiments). Nevertheless, the largest (and irreversible) effects on the followed XRD lattice spacings occur during the various phase transitions and excursions in temperature and pressure around the critical point. However, we also note that the Ni-BpyMe XRD peaks that do not change in lattice spacing on gas sorption under subcritical gas pressures still do not exhibit lattice-spacing changes under the more extreme conditions of the supercritical regime. Some of the irreversible structural changes that do occur coincide with more reversible but significant increases and decreases in the nanoscale porosity. While much of this is beyond the scope of the present DFT predictions, the DFT-predicted orientational changes in the ligands during gas adsorption suggest some irreversible trapping of CO₂ molecules is possible. Overall, our observations also suggest that supercritical CO₂ can play an activating solvent role in the use of advanced sorbents in catalysis and other applications.

We conclude by noting the increasing importance of MOFs and other related sorbent materials, including the PICNIC series, for a range of applications across catalysis, enhanced gas recovery, carbon mitigation, *i.e.* carbon dioxide reduction

(CDR), and even direct air capture (DAC) of CO₂. Various adsorption/desorption isotherm and gas breakthrough measurements are in increasing demand for assessing the performance of these advanced sorbents. However, the complexity of the material design required to optimize the materials for a given gas sorption or separation function creates a need for *in situ* or *operando* measurements such as those utilizing XRD and SAXS methods as described here, to be coupled with and validate computational modeling and DFT calculations. This will be essential in elucidating the complex gas sorption phenomena to be exploited if the full potential of these materials is to be realized and the most optimal materials are to be selected for scale-up for industrial use, while also taking into account the need to reduce the costs of synthesis, processing and placement.

Acknowledgements

We thank Dr Jan Ilavsky of X-ray Science Division, Argonne National Laboratory, Argonne, IL, USA, for X-ray beam line support, especially in regard to the dual gas flow measurements using the Hidden XCS system.

Funding information

This research used resources of the Advanced Photon Source, a US Department of Energy (DOE) Office of Science User Facility operated for the DOE Office of Science by Argonne National Laboratory under contract No. DE-AC02-06CH11357.

References

- Adil, K., Belmabkhout, Y., Pillai, R. S., Cadiau, A., Bhatt, P. M., Assen, A. H., Maurin, G. & Eddaoudi, M. (2017). *Chem. Soc. Rev.* **46**, 3402–3430.
- Allen, A. J., Espinal, L., Wong-Ng, W., Queen, W. L., Brown, C. M., Kline, S. R., Kauffman, K. L., Culp, J. T. & Matranga, C. (2015). *J. Alloys Compd.* **647**, 24–34.
- Allen, A. J., Wong-Ng, W., Cockayne, E., Culp, J. & Matranga, C. (2018). *Nanomaterials*, **9**, 354.
- Banerjee, D., Wang, H., Plonka, A. M., Emge, T. J., Parise, J. B. & Li, J. (2016). *Chem. Eur. J.* **22**, 11816–11825.
- Bennett, T. D. & Cheetham, A. K. (2014). *Acc. Chem. Res.* **47**, 1555–1562.
- Chantler, C. T., Olsen, K., Dragoset, R. A., Chang, J., Kishore, A. R., Kotochigova, S. A. & Zucker, D. S. (2005). *X-ray Form Factor, Attenuation, and Scattering Tables*. Version 2.1. NIST, Gaithersburg, Maryland, USA. <https://www.nist.gov/pml/x-ray-form-factor-attenuation-and-scattering-tables>.
- Cockayne, E. (2019). *Powder Diffraction*, **34**, 227–232.
- Cockayne, E., Wong-Ng, W., Chen, Y.-S., Culp, J. T. & Allen, A. J. (2021). *J. Phys. Chem. C*, **125**, 15882–15889.
- Coudert, F.-X. (2015). *Chem. Mater.* **27**, 1905–1916.
- Culp, J. T., Madden, C., Kauffman, K., Shi, F. & Matranga, C. (2013). *Inorg. Chem.* **52**, 4205–4216.
- Culp, J. T., Sui, L., Goodman, A. & Luebke, D. (2013). *J. Colloid Interface Sci.* **393**, 278–285.
- Férey, G. (2008). *Chem. Soc. Rev.* **37**, 191–214.
- Ferreira, T. J., Vera, A. T., de Moura, B. A., Esteves, L. M., Tariq, M., Esperança, J. M. S. S. & Esteves, I. A. A. C. (2020). *Front. Chem.* **8**, 590191.
- Groom, C. R., Bruno, I. J., Lightfoot, M. P. & Ward, S. C. (2016). *Acta Cryst. B* **72**, 171–179.
- Hagman, D., Hagman, P. J. & Zubieta, J. (1999). *Angew. Chem. Int. Ed.* **38**, 3165–3168.
- Hofmann, K. A. & Küspert, F. (1897). *Z. Anorg. Chem.* **15**, 204–207.
- Humphrey, W., Dalke, A. & Schulten, K. (1996). *J. Mol. Graph.* **14**, 33–38.
- Ilavsky, J. (2012). *J. Appl. Cryst.* **45**, 324–328.
- Ilavsky, J. & Jemian, P. R. (2009). *J. Appl. Cryst.* **42**, 347–353.
- Ilavsky, J., Zhang, F., Andrews, R. N., Kuzmenko, I., Jemian, P. R., Levine, L. E. & Allen, A. J. (2018). *J. Appl. Cryst.* **51**, 867–882.
- Kauffman, K. L., Culp, J. T., Allen, A. J., Espinal, L., Wong-Ng, W., Brown, T. D., Goodman, A., Bernardo, M. P., Pancoast, R. J., Chirdon, D. & Matranga, C. (2011). *Angew. Chem. Int. Ed.* **50**, 10888–10892.
- Kresse, G. & Furthmüller, J. (1996a). *Comput. Mater. Sci.* **6**, 15–50.
- Kresse, G. & Furthmüller, J. (1996b). *Phys. Rev. B*, **54**, 11169–11186.
- Momma, K. & Izumi, F. (2008). *J. Appl. Cryst.* **41**, 653–658.
- Potton, J. A., Daniell, G. J. & Rainford, B. D. (1988). *J. Appl. Cryst.* **21**, 663–668.
- Sing, K. S. W. (1985). *Pure Appl. Chem.* **57**, 603–619.
- Span, R. & Wagner, W. (1996). *J. Phys. Chem. Ref. Data*, **25**, 1509–1596.
- Trickett, C. A., Helal, A., Al-Maythaly, B. A., Yamani, Z. H., Cordova, K. E. & Yaghi, O. M. (2017). *Nat. Rev. Mater.* **2**, 17045.
- Wong-Ng, W., Culp, J. & Chen, Y.-S. (2016). *Crystals*, **6**, 108.
- Wong-Ng, W., Culp, J., Siderius, D. W., Chen, Y., Wang, S. Y. G., Allen, A. J. & Cockayne, E. (2021). *Polyhedron*, **200**, 115132.
- Wong-Ng, W., Culp, J. T., Chen, Y. S., Zavalij, P., Espinal, L., Siderius, D. W., Allen, A. J., Scheins, S. & Matranga, C. (2013). *CrystEngComm*, **15**, 4684–4693.
- Yaghi, O. M., O’Keeffe, M., Ockwig, M. W., Chae, H. K., Eddaoudi, M. & Kim, J. (2003). *Nature*, **423**, 705–714.